Journal of Geophysical Research: Planets

RESEARCH ARTICLE
10.1029/2018JE005723

Eolianite Grain Size Distributions as a Proxy for Large Changes in Planetary Atmospheric Density

Erik A. Goosmann[1], David C. Catling[1], Sanjoy M. Som[2], Wladyslaw Altermann[3], and Roger Buick[1]

[1]Department of Earth and Space Sciences and Astrobiology Program, University of Washington, Seattle, WA, USA, [2]Blue Marble Space Institute of Science, Seattle, WA, USA, [3]Department of Geology, University of Pretoria, Pretoria, South Africa

Key Points:
- Lower air density could increase the mean grain size of windblown sand dunes by affecting air drag and path lengths of grains in the air
- Precambrian eolianites show no mean size change from modern dunes, despite data showing lower air density on the Earth in the Neoarchean
- An order of magnitude air density change is probably required to change mean grain size clearly, making Mars a better place to use this method

Supporting Information:
- Supporting Information S1
- Supporting Information S2

Correspondence to:
E. A. Goosmann,
goosmann@uw.edu

Citation:
Goosmann, E. A., Catling, D. C., Som, S. M., Altermann, W., & Buick, R. (2018). Eolianite grain size distributions as a proxy for large changes in planetary atmospheric density. *Journal of Geophysical Research: Planets*, *123*, 2506–2526. https://doi.org/10.1029/2018JE005723

Received 14 JUN 2018
Accepted 1 AUG 2018
Accepted article online 19 SEP 2018
Published online 8 OCT 2018

Abstract Atmospheres are dynamic over geologic timescales, making large changes in planetary air density possible. For the Earth, geological proxies suggest that air density in the Neoarchean was similar to or lower than today. This air density variation possibly affected eolian dune grain sizes by controlling the trajectories of grains though the air. Balancing the fall velocity and threshold friction velocity, a metric separating saltation and suspension transport, suggests that a lower air density could increase the mean grain size of dunes because decreased air drag extends the size range of grains in modified saltation and incipient suspension regimes. Consequently, the dune-forming sand left behind in pure saltation, the dominant dune-forming transport mode, could have coarser grains. We analyzed size distributions of two eolianites from 2.64 and 1.5 Ga (billion years ago) for deviations from modern sand dunes emplaced at sea level, which globally exhibit similar mean grain sizes. Both aeolianites have mean grain sizes within one standard deviation of the modern mean and are not statistically separable at 95% confidence. Overall, this suggests that while air density is important in eolian physics, a factor of 2 to 4 change in density is insufficient to produce an unambiguous grain size signal. This suggests that while eolian dune grain sizes have not significantly changed over the range of Earth's atmospheric conditions, they could be useful when investigating the order of magnitude changes thought to have occurred on Mars.

Plain Language Summary The atmospheres of planets can change dramatically through time, and 2.7 billion years ago Earth's atmosphere may have been thinner than it is today. One geological process that might record this change is windblown sand dunes. A thinner atmosphere could shift the size ranges of sand in windblown transport and would overall increase the grain sizes in wind-formed sand dunes because there is less air drag when sand grains travel through the wind. We looked at two ancient windblown sandstones to see if there was any significant change in grain sizes. Neither showed a difference from modern sand dunes, and it is probable that larger air pressure changes than available on the Earth (past or present) are needed to see a difference in grain sizes. As a result, this method may only work on planets where air density fluctuations are several orders of magnitude, such as Mars.

1. Introduction

Atmospheric density on Earth may have changed over the planet's 4.5 billion year history. Before the Great Oxidation Event (GOE) at ~2.4–2.2 Ga, oxygen, which is 21% of Earth's current atmosphere, was below one millionth the present atmospheric level (Bekker et al., 2004; Zahnle et al., 2006). This could mean that nitrogen was the key bulk atmospheric constituent in the Archean. While recent carbon cycle modeling indicates that temperate Archean temperatures are possible with higher levels of CO_2 and CH_4 within current atmospheric constraints (Krissansen-Totton et al., 2018), higher nitrogen partial pressures of 2–3 bar in the Archean could have enhanced greenhouse warming through pressure broadening of greenhouse gas absorption lines, keeping the Earth warm despite the young Sun's lower luminosity (Goldblatt et al., 2009). The hypothesis of more Archean atmospheric nitrogen has lead others to look for geological proxies for air pressure in deep time.

Unfortunately, there are very few geologic processes that record ancient atmospheric pressure and density, but three methods used include fossilized raindrop imprints (Som et al., 2012), $N_2/^{36}Ar$ in quartz fluid inclusions (Avice et al., 2018; Marty et al., 2013), and basalt vesicle volume ratios (Som et al., 2016). These geologic proxies suggest that late Archean atmospheric pressure was no more than modern pressure (Avice et al., 2018; Marty et al., 2013; Som et al., 2012) and maybe as low as 0.50–0.25 bar (Som et al.,

2016). However, these proxies do not agree with some models of nitrogen cycling based on modern subduction fluxes, which imply that atmospheric pressure has monotonically decreased over time (Johnson & Goldblatt, 2015; Mallik et al., 2018). More data from multiple geological proxies would provide valuable empirical constraints for such models.

Air density has been considered when comparing eolian transport of sand on Earth, Venus, Titan, Mars, and Pluto (e.g., Greeley & Iversen, 1985; Kok et al., 2012; Telfer et al., 2018). Changes in atmospheric conditions, including air pressure and density, measurably affect eolian bedforms. Eolian dune and ripple wavelengths scale with the reciprocal of air density (Claudin & Andreotti, 2006), which Lorenz et al. (2014) observed from dunes spanning 23-km in elevation and nearly an order of magnitude change in atmospheric pressure and density on Tharsis Mons, Mars. Grain size increase with elevation could also factor in to the Martian bedform wavelength changes (Lorenz et al., 2014). Based on the balancing of aerodynamic and inertial grain forces, changes in air density and gravity could affect the transportable grain sizes for dunes on other planets (Edgett & Christensen, 1991; Greeley & Iversen, 1985, p. 70). Modern eolian quartz dunes on Earth cluster around a mean grain size of 200–220 μm with a 1σ spread of 75 μm (Ahlbrandt, 1979; Goudie et al., 1987). If transport conditions changed during Earth's history due to air density fluctuations, statistical measures of ancient dune grain size distributions (i.e., mean, sorting, skewness, and kurtosis) and deviations from modern ranges may provide a first order indicator of these differences.

The physics describing eolian movement was pioneered by Bagnold (1941) and later expanded using low pressure wind tunnel observations by Iversen and White (1982) and Greeley and Iversen (1985). Kok et al. (2012) provide a comprehensive review. Here we first discuss the current state of paleoatmospheric pressure constraints and summarize the pertinent physics of eolian transport and its link to air density change. Then we apply this knowledge to two Precambrian eolianites from 2.64 Ga and 1.5 Ga to investigate the possibility of eolian response to barometric pressure and density change through geologic time.

2. Atmospheric Density in the Archean

Geologic proxy measurements and many nitrogen cycle models disagree on Precambrian atmospheric pressure and density. With nitrogen as possibly the most important gas in the Precambrian, many models assume a 1 bar atmosphere of nitrogen by increasing the current partial pressure of nitrogen (~0.8 bar) by 0.2 bar to make up for the absence of O_2. Precambrian nitrogen abundance inferred from $N_2/^{36}Ar$ ratios in fluid inclusions constrains the upper limit on nitrogen partial pressure to 0.5–1.1 bar at ~3.5 Ga (Marty et al., 2013) and ~0.5–1 bar (2σ upper bound) at 3.3 Ga (Avice et al., 2018, their Figure 4a). Raindrop crater sizes indicate the upper limit to air pressure was likely 0.52–1.1 bar at ~2.7 Ga (Som et al., 2012). These two proxy methods calculate probable upper limits, and absolute pressure at ~2.7 Ga from vesicle volume ratios in Archean subaerial basalts was calculated to be 0.25–0.50 bar (Som et al., 2016). These proxies indicate that air pressure in the late Archean was probably lower than today.

Some models disagree with these findings. Studies have found a mantle nitrogen abundance of 7 ± 4 times the present atmospheric level (Johnson & Goldblatt, 2015) and coupled with modern subduction recycling rates (Mallik et al., 2018), these imply that the mantle is a long-term sink of atmospheric nitrogen that has been monotonically sequestered over time. However, modern fluxes only apply if redox conditions were constant through time, yet models including nitrogen speciation change indicate that redox has a substantial effect on the atmospheric reservoir (Laneuville et al., 2018; Stüeken et al., 2016). The stable form of deep sea nitrogen for the Archean would have been NH_4^+ (Holland, 2002), not oxidized species like NO_3^- as in modern oceans. NH_4^+ readily substitutes for K^+ in clay minerals, meaning it could accumulate in marine sediments and be subducted over time (Som et al., 2016). Additionally, NH_4^+ could be stored directly in the dissolved ocean reservoir (Laneuville et al., 2018). The lack of oxygen before the GOE inhibited nitrification, denitrification, and then liberation of N_2 back to the atmosphere, and so nitrogen could accumulate in the ocean, crust, and mantle.

At the GOE, NO_3^- became the dominant marine nitrogen species and nitrogen could return to the atmosphere through denitrification. This is an atmospheric source that was originally absent, causing air pressure to increase from pre-GOE levels. A monotonic drawdown theory of pressure assuming current

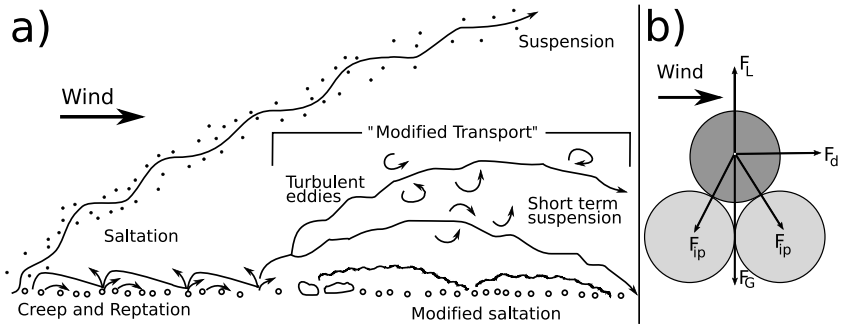

Figure 1. (a) Illustration of eolian transport styles. Following Pye (1987) and Kok et al. (2012). (b) Illustration of the forces acting on a spherical grain on a bed of spherical grains. F_L = lift force, F_d = drag force, F_G = grain weight, and F_{ip} = interparticle cohesive force. Following Kok et al. (2012).

subduction fluxes needs to consider this change in redox-sensitive nitrogen speciation. In particular, an important nitrogen flux back to the atmosphere after the GOE would come from oxidative weathering of crustal materials. The main long-term source of nitrate for denitrification to N_2 would be oxidative weathering of organic matter as it is today (Berner, 2006). Oxidative weathering of clays and micas that contain reduced nitrogen species, deposited before atmospheric oxygenation, would also provide a nitrate source for denitrification. Thus, atmospheric density is more likely to have risen than fallen in the aftermath of the GOE.

The Som et al. (2012) raindrop method was criticized by Kavanagh and Goldblatt (2015), who argued that the upper limit on Archean pressure should be extended to ~10 bar. This was justified by increasing the maximum terrestrial raindrop size to 10 mm from 6.8 mm based on a data set that was a subset of a larger data repository with >240 million modern raindrop measurements (see Gatlin et al., 2015). In the repository created by Gatlin et al., 0.4% of drops measured were >5 mm in diameter, with only 41 of 240 million > 8 mm and 4 > 9 mm. These large raindrops, which are exceptionally rare, occurred beneath hail-producing clouds and were evidently resulted from hail that completely melted just prior to reaching the ground (Gatlin et al., 2015). This is consistent with aerodynamic forces significantly reducing the average life of drops larger than 7 mm (Komabayasi et al., 1964). Thus, the 6.8 mm upper limit of raindrop sizes and upper bound pressure constraint of 0.5–1.1 bar by Som et al. (2012) is likely valid given the statistically miniscule chance that 2.7-Ga raindrop imprints on 18 distinct bedding surfaces somehow all happened to sample the extremely rare occurrence of hail that had just melted before hitting the ground.

Considering the current geological proxy measurements, following the empirical data indicates that late Archean atmospheric pressure was maybe as low as 0.25–0.50 bar with an upper limit equal to modern pressure. We use this baseline to investigate whether eolian processes at 2.64 and 1.5 Ga were measurably affected by different air density.

3. The Physics of Eolian Transport

Sand dunes form in both aqueous and eolian environments, the latter being affected by air density. The primary ways eolian sand moves are suspension, saltation, creep, and reptation (Figure 1a). Suspension occurs when grains are entrained in the air and travel long distances. Saltation occurs when sand grains hop on parabolic arcs, ballistically fall and collide with the bed, and eject other grains into motion. Creep occurs when large grains roll across the bed surface. Reptation, which is similar to creep, is when larger grains hop across the surface no farther than a few grain diameters and do not have enough kinetic energy to dislodge other grains into motion (Kok et al., 2012).

The eolian transport regime depends on wind speed, grain size, gravity, interparticle cohesion, and air density. Coarse material creeps and reptates due to higher inertia and is too large to dominate the transport flux. Most clay and silt is suspended long term and does not settle to form dunes (Kocurek, 1996; Lancaster, 1995).

While some suspended grains fall out on the lee slopes of dunes and contribute the smallest grain sizes, the dominant constituents are saltating grains, which are primarily composed of fine and medium-grained sand (<500 μm). Air density change could modify grain sizes in dunes by altering the upper grain size limit for entering saltation and suspension.

The wind selectively transports a small grain size range due to the much lower density and viscosity of air versus the grains being moved. Water sorts grains as well, but the higher viscosity of water allows it to transport a larger range of sizes. Despite variable source supply and wind regimes, most eolian dune sand is between 100 and 300 μm in diameter (Kocurek, 1996). Specifically, the data of Ahlbrandt (1979) from ~450 dune samples shows that quartz dunes at sea level have average mean grain sizes of 220 ± 75 μm (1σ) and are skewed toward smaller sizes, although it should be noted that the spread is wide and the mean reaches 660 μm at the Sabha dunes in Libya (Appendix A). Goudie et al. (1987) presented a similar finding with 1,261 quartz dune samples averaging 202 ± 42 μm (1σ). End-member controls on dune grain size include air properties, grain properties, source area, and wind regime. Examining mean grain sizes of dunes formed in a variety of air densities could provide evidence of a measurable relationship between air density and grain size distribution that could be used as a paleoatmospheric pressure proxy.

Eolian sediment transport relies on the physical relationship between fluid forces and the material properties of transported grains. For an idealized spherical grain at rest, the forces acting on the grain are fluid lift, fluid drag, grain weight, and interparticle cohesion (Figure 1b). Lift and drag are aerodynamically controlled, while weight and cohesion are material properties. For a grain to be directly moved by the wind, fluid forces must overcome inertial forces. However, it should be noted that in natural environments, other parameters such as surface roughness and grain nonsphericity both affect grain movement.

For an average wind speed ($\overline{u}$) at height z above the bed, the *law of the wall* gives the time-averaged wind profile near the bed (Bagnold, 1941)

$$\overline{u} = (u_*/\kappa)\ln(z/z_o) \tag{1}$$

where κ is the von Kármán's constant (≈ 0.41) and z_o is the roughness length, which is a lower boundary height above the bed where zero velocity occurs (generally smaller for smoother surfaces). The wind friction velocity (u_*) is a time-averaged wind speed that is invariant with height. The friction velocity is related to shear stress (τ) near the bed for a given air density (ρ_a).

$$u_* = (\tau/\rho_a)^{1/2} \tag{2}$$

For each grain diameter there is a threshold friction velocity (u_{*t}) required for movement to begin as a result of wind shear. A commonly used formulation by Shao and Lu (2000) balances shear forces with inertial forces to give

$$u_{*t} = \sqrt{A_N\left(\sigma_\rho g d + \frac{\gamma}{\rho_a d}\right)} \tag{3}$$

with A_N as a dimensionless constant of 0.0123 (Shao & Lu, 2000), g as the gravitational constant (9.8 m/s^2 on Earth), and σ_ρ as the ratio of rock to air density. Here cohesion is scaled by particle diameter (d) and a proportionality constant (γ). Shao and Klose (2016) showed that $\gamma = 1.5 \times 10^{-4}$ N/m fits the data of Greeley and Iversen (1985). Cohesion may change for different gravities due to low gravity decreasing overall soil compression (Musiolik et al., 2018).

The other term related to saltation is the fall velocity (u_F). There are a variety of empirical expressions for this parameter, each varying based on a formulation of the drag coefficient as a function of fluid and grain properties. While originally created for water, the empirical equation by Ferguson and Church (2004), as modified by Jerolmack et al. (2006) for air, works for a variety of natural sands

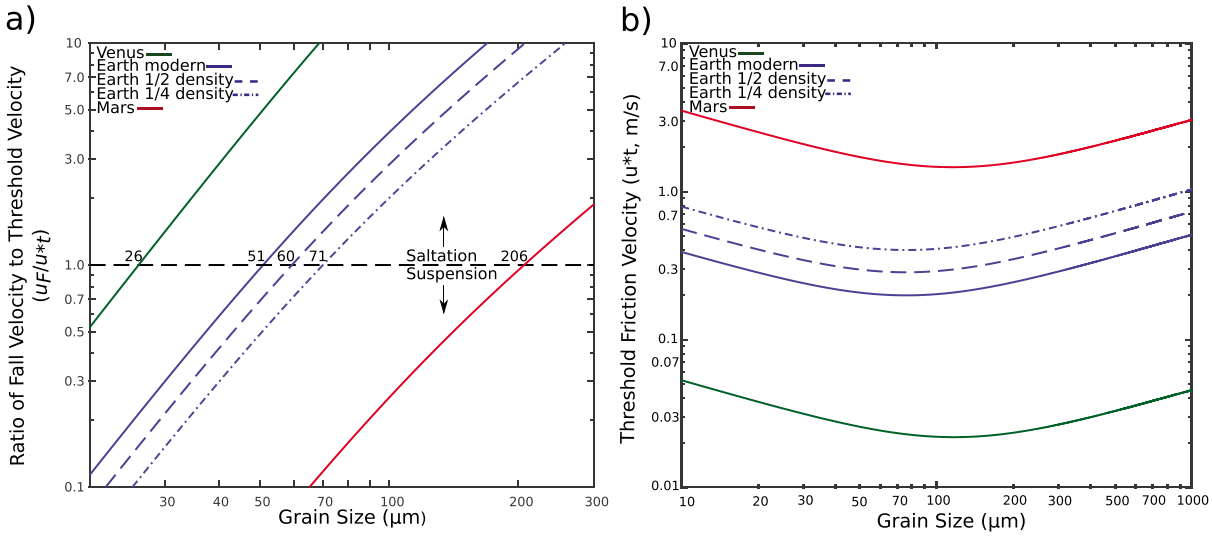

Figure 2. (a) Ratio of the terminal fall velocity (u_F) to threshold friction velocity (u_{*t}) for various planetary conditions. Grain size at $u_F/u_{*t} = 1$ is the grain size in modified transport. Similar to Greeley and Iversen (1985). (b) Threshold friction velocity (u_{*t}) as a function of grain size for various planetary conditions. Venus = green, modern earth = solid blue, ½ density earth = dashed blue, ¼ density earth = dot-dashed blue, Mars = red.

$$u_F = \frac{(\sigma_\rho - 1)gd^2}{C_1 v + \left(0.75 C_2 \left((\sigma_\rho - 1)gd^3\right)^{1/2}\right.} \tag{4}$$

where C_1 is a dimensionless constant of 18 and C_2 represents the asymptotic value of the drag coefficient (≈ 1 for typical sand grains).

The u_F/u_* ratio has traditionally been regarded as separating saltation and suspension (Eastwood et al., 2012; Edgett & Christensen, 1991; Greeley & Iversen, 1985; Jerolmack et al., 2006; Pye & Tsoar, 1990; Sullivan & Kok, 2017). The transport type for a given grain depends on whether the downward velocity of the grain (u_F) exceeds or is below mean vertical turbulent dispersion (~u_*; Bagnold, 1966; Eastwood et al., 2012; Jerolmack et al., 2006 ; Shao, 2008). Pure saltation is seen at $u_F/u_* > 2$–5 and pure suspension at $u_F/u_* < 0.1$ (Jerolmack et al., 2006; Shao, 2008), implying that the boundary is transitional. This transitional transport regime at $0.1 < u_F/u_* < 2$ occurs when saltating grains are significantly affected by vertical eddy turbulence and combines the two modes of incipient suspension and modified saltation (Figure 1a), hereafter referred to as modified transport.

Bagnold (1966) identified the onset of suspension susceptibility when $u_F/u_* = 1$ due to the visually observed development of a measurable concentration of suspended sediment. We follow this definition by identifying the start of modified transport conditions when $u_F/u_{*t} = 1$, which was verified through modeling by Sullivan and Kok (2017). Here u_* is replaced by u_{*t}, thus indicating the mode of transport when grains initially move at their threshold speed.

Plotting the ratio of u_F/u_{*t} as a function of particle diameter for different planetary conditions provides a first-order assessment of grain sizes for eolian dunes (Figure 2a). This was originally done by Greeley and Iversen (1985) as a relative size predictor for Venus, Earth, and Mars. Venus has a lower u_F/u_{*t} boundary grain size, and Mars has an order of magnitude larger boundary grain size, suggesting finer and coarser grained dunes respectively for these planetary bodies when sand is mobilized by the wind.

Figure 2a also shows u_F/u_{*t} for grains on Earth with air densities of 1.0, 0.5, and 0.25 times modern levels—the ranges of three Archean paleobarometers (section 2; Avice et al., 2018; Marty et al., 2013; Som et al., 2012, 2016). The increase at the boundary size between the three air densities is on the order of ~20 μm. This can be contrasted with the threshold friction velocity for a given grain diameter (Figure 2b), which is

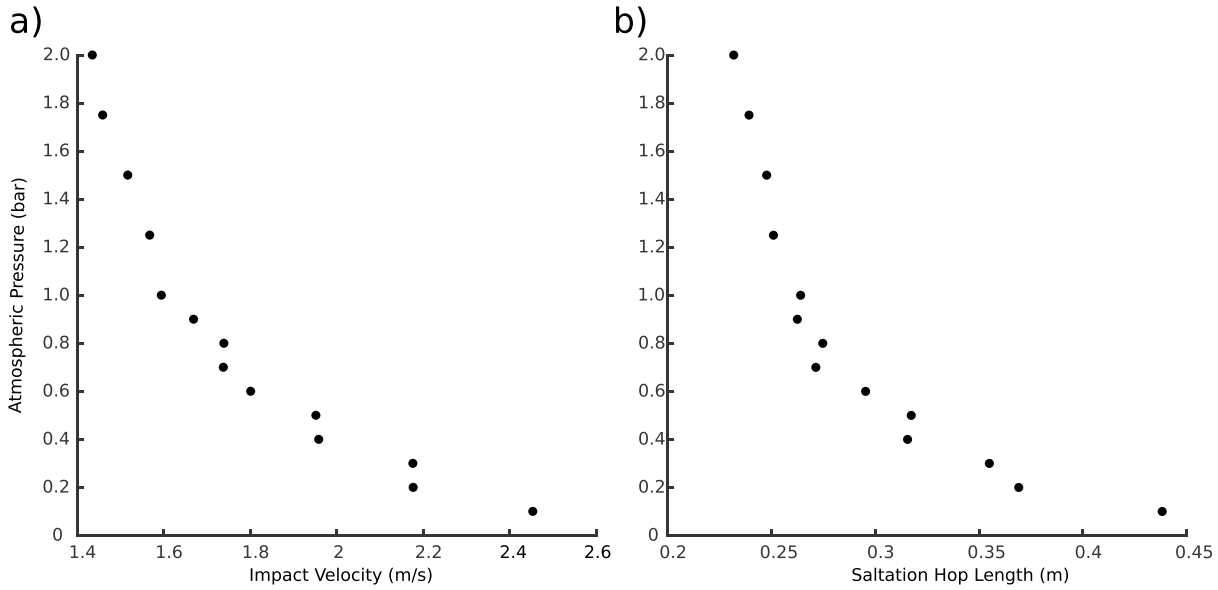

Figure 3. Response of saltator impact velocity (a) and saltation path length (b) with air density. As density decreases, the ballistic trajectory of saltating grains lengthens and the impact velocity similarly increases. Calculations were made using COMSALT (Kok & Renno, 2009) at a constant friction velocity of 0.5 m/s.

higher for decreasing air density. Both graphs shift with changing air density suggesting that such change could have a measurable effect on grain sizes in eolian transport.

Threshold conditions are usually different from the conditions producing mean values, thus making the determination of a scaling law that fits aerodynamic and grain properties to the observed mean grain size for dunes difficult. So far no such scaling law has been developed. Also, Figures 2a and 2b produce competing models. Figure 2a suggests that grain sizes should increase when atmospheric density decreases, due to the reduced drag from a less dense atmosphere increasing grain sizes in modified transport (e.g., Edgett & Christensen, 1991; Greeley & Iversen, 1985). However, this requires that the grains are already moving, which is harder to initiate due to reduced lift and the increased fluid threshold friction velocity (Figure 2b). Consequently, the argument is that when periodic gusts exceed the threshold velocity, the size range for grains going into suspension is extended, which leaves behind coarser grains in the saltating dune-forming sand (Edgett & Christensen, 1991).

Advances in eolian transport theory highlight hysteresis as reducing the effect of this increased fluid threshold friction velocity on saltation transport on Mars (e.g., Kok, 2010; Sullivan & Kok, 2017). Once saltation starts for a small number of grains, it propagates downwind and is sustained at wind speeds below the fluid threshold due to grain splashing. This effect is important in eolian systems because energy transfer from particle impacts is more efficient than fluid drag once grains are moving (Kok et al., 2012). This means that saltation can be maintained at lower wind speeds after an initial gust of wind reaches the fluid threshold and that many grains begin moving through splash processes. The wind velocity for sustained transport once moving is the *impact threshold* and is ~80% of the fluid threshold for the modern Earth (Bagnold, 1941) and ~10% for Mars (Kok, 2010). Additionally, wind speed fits a Weibull distribution (Lorenz, 1996), with a higher probability of low wind speed events and decreasing probability of events above the fluid threshold. During low-frequency, high wind-speed events in thin atmospheres like Mars, small sand fluxes propagate downwind as sand clusters due to the extremely low impact threshold (Sullivan & Kok, 2017). Thus, saltation and dune formation still occurs even if fluid threshold velocities are high.

We modeled steady state saltation grain trajectories with air density change using the numerical saltation model COMSALT (Kok & Renno, 2009). For a constant wind speed above the bed, Figure 3 shows that as atmospheric density decreases, both the impact velocity of saltators onto the bed (Figure 3a) and the saltation path length (Figure 3b) increase. Larger impact velocities would facilitate grain splash and

propagate saltation downwind for large grains. Longer saltation path lengths would increase the time that grains are in the air relative to modern values, increasing the susceptibility to suspension (e.g., Edgett & Christensen, 1991). Both of these would work to move larger grains out of pure saltation and into a modified transport regime in which upward turbulence significantly affects grain paths.

The ratio of the fall velocity over friction velocity as a boundary between saltation and suspension is an established concept in the literature (e.g., Edgett & Christensen, 1991; Greeley & Iversen, 1985). If transport properties are a dominant control on grain sizes, once grains are moved either by a low-frequency, high speed gust of wind or particle splash from an already-moving grain, the increased impact velocity and saltation distance expected for lower air density (Figure 3a and 3b) could make larger grains become more susceptible to modified transport with longer path lengths. This could ultimately coarsen the sands remaining in pure saltation, which are the dominant dune-forming grains.

Given our predicted coarsening under low air density, investigating the grain sizes of lithified Archean eolian dunes should show whether eolian processes measurably change for air density fluctuations within current likely late-Archean constraints (from 1 down to 0.25 bar). Thus, we examined two ancient eolianites, the ~2.64-Ga Vryburg Formation in South Africa (Altermann et al., 2014) and the ~1.5-Ga Nipigon Bay Formation in Canada (Rogala et al., 2005). Fossil raindrops and lava vesicle size ratios suggest a lower atmospheric pressure at the time of deposition of the Vryburg Fm. (Som et al., 2012, 2016), but there is currently no proxy constraint for pressure during the time of deposition of the Nipigon Bay Fm. or indeed at any time in the Proterozoic.

4. Geologic Context

4.1. The Vryburg Formation

The Vryburg Formation in South Africa is the lowermost unit of the Schmidtsdrif Subgroup in the Griqualand-West basin of the Transvaal Supergroup (Figure 4). A zircon age of 2,642 Ma is widely accepted as the minimum age (Walraven & Martini, 1995). The Vryburg Fm. ranges from 10- to 250-m thick and includes slightly metamorphosed basal conglomerates, quartzites, shales, and carbonates. Overlying the Vryburg Fm. is the middle and upper part of the Schmidtsdrif Subgroup, which is comprised of Boomplas Formation stromatolitic and oolitic platform carbonates and Clearwater Formation shales (Eriksson et al., 2006). The ~300-m Schmidtsdrif Subgroup is interpreted as recording the initial flooding of the Kaapvaal Craton and subsequent basin deepening (Schröder et al., 2006). The basal conglomeratic section of the Vryburg Fm. lies unconformably atop its source Ventersdorp Supergroup volcanics. The Vryburg Fm. contains cross-stratified orthoquartzites interpreted as eolian (Altermann et al., 2014). Well-exposed outcrops are available within an abandoned quarry near Prieska, South Africa (S29.33693°, E022.30536°). Sedimentary structures include tabular crossbed sets up to 20-m long and 3-m tall with high-angle foresets (Figure 5a), preserved toesets (Figure 5b), and basal erosional surfaces overlain by symmetrical low-index ripples, grainflow structures, and horizontal millimeter-scale laminae (Figure 5c). There is a lack of distinctive fluvial features such as gutter casts and flute marks.

4.2. The Nipigon Bay Formation

The 1450–1500 Ma Sibley Group is a Mesoproterozoic sedimentary sequence deposited in a subsiding intracratonic basin (Rogala et al., 2005; Rogala et al., 2007). Exposures are on the northwest shore of Lake Superior in Ontario, Canada (Figure 6). In the central Sibley basin, sedimentary rocks are thermally metamorphosed up to 400–500 °C by intrusive diabase sills. However, metamorphism is localized (Rogala et al., 2005) and a majority of the rocks are diagenetically altered, but unmetamorphosed. Beginning at the base, the sequence includes braided stream sediments (Pass Lake Formation); transgressive lacustrine siliciclastics, evaporative and stromatolitic saline lacustrine carbonates, and sabkha and saline mudflat deposits (Rossport Formation); and prograding deltaic shales (Kama Hill Formation) grading into braided mouth bar and channel sediments (Outan Island Formation). Overlying the cap-deltaic Outan Island Formation and atop an angular unconformity is the Nipigon Bay Formation, a ~450-m section of cross-stratified sandstone consisting of alternating high-angle and low-angle tabular crossbeds recognized as eolian (Rogala et al., 2005; Rogala et al., 2007). It is principally visible in drill core, and the only outcrop exposure found on Simpson Island contains a 15-m high relict dune form with high-angle foresets (Figure 5d), preserved toesets (Figure 5e), curved and planar reactivation surfaces (Figure 5f), and rare preserved ripple forms (Rogala et al., 2007).

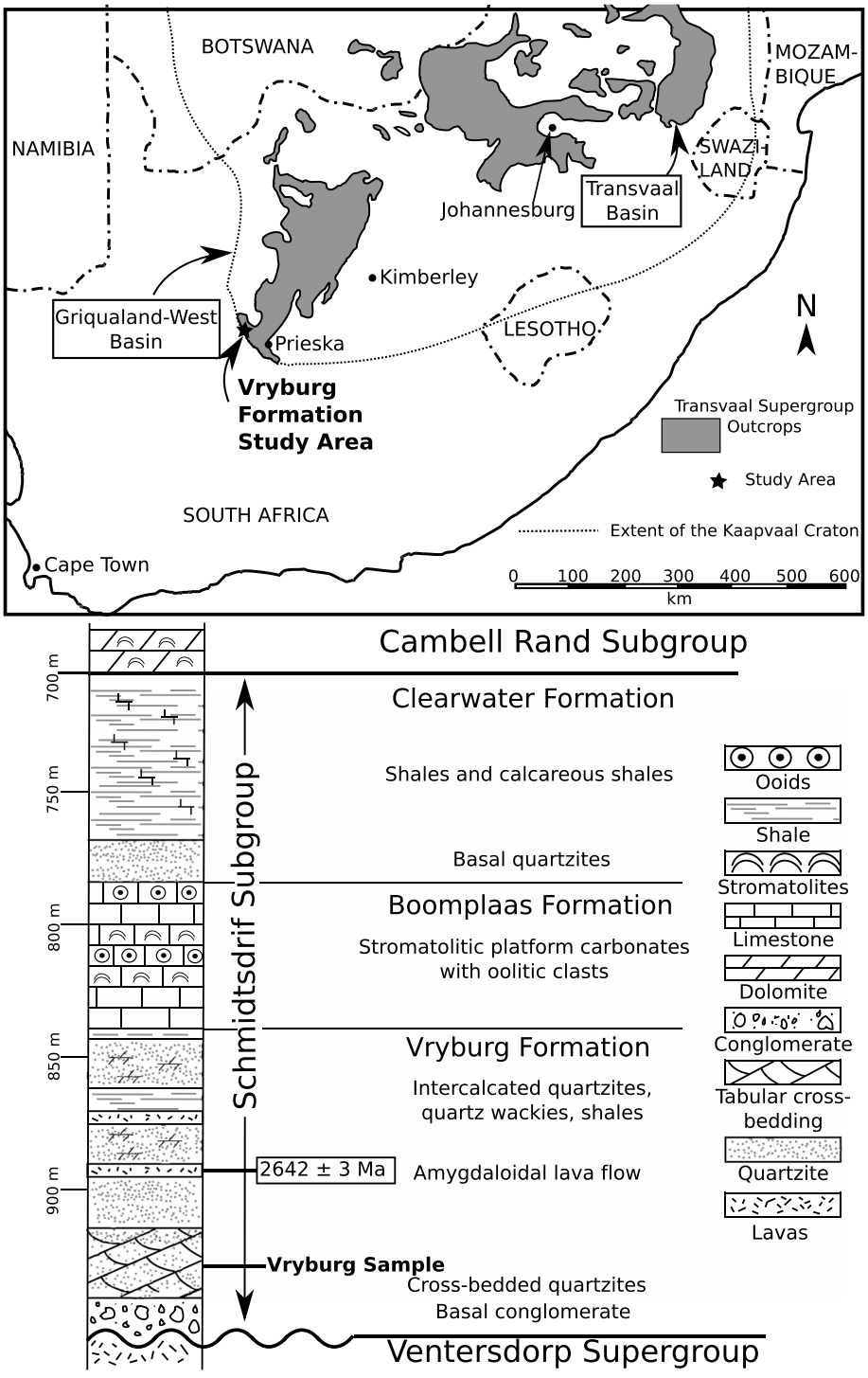

Figure 4. Distribution of the Transvaal Supergroup and the generalized stratigraphic column of the Schmidtsdrif Subgroup in the Griqualand-West Basin. Column thicknesses are generalized due to variable thicknesses at different sites. Column and map based on data from the South African Committee for Stratigraphy (Altermann & Nelson, 1998; Eriksson et al., 2006).

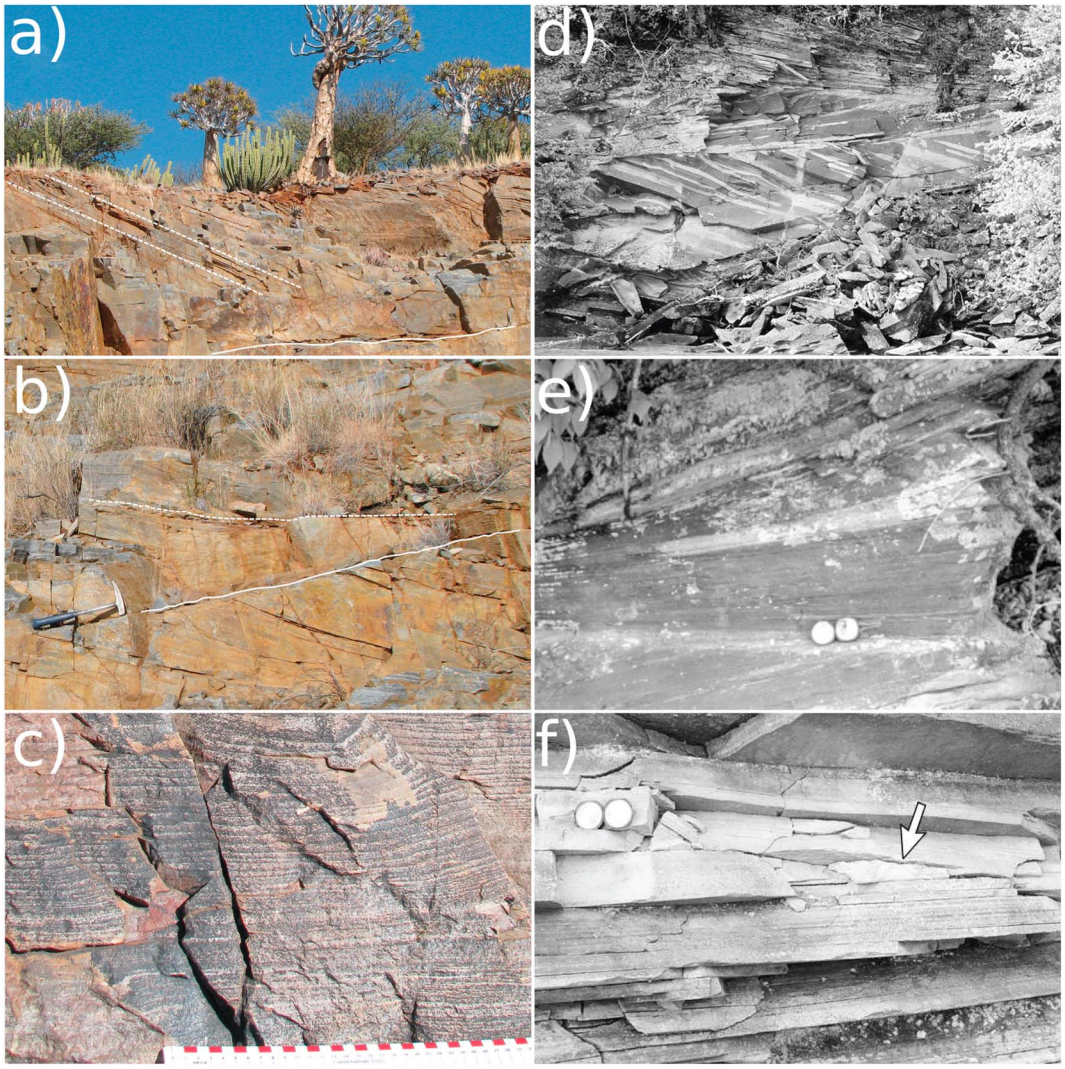

Figure 5. (a) Vryburg Fm. tabular crossbed set. Dashed white lines show foresets and solid white line shows the base of the set. Tree is ~3.5 m. (b) Vryburg Fm. Toeset. The 41-cm long hammer is lying atop basal erosional contact. (c) Vryburg Fm. Mm-scale horizontal laminae. Ruler is centimeter scale. (d) Nipigon Bay Fm. High-angled foresets. Individual sets range from 50- o 350-cm thick, with an average of 100 cm (Rogala et al., 2005). (e) Nipigon Bay Fm. Preserved toeset. (f) Nipigon Bay Fm. Reactivation surface (arrow). Brunton compass for scale in e and f is ~15 cm long. Photo credit: (a–c) W. Altermann and (d–f) P. Fralick.

5. Materials and Methods

Representative thin sections cut normal to bedding were studied using an Olympus BX53 petrographic microscope, and images were taken at 4X magnification with an Olympus DP22 camera. The Vryburg Fm. was sampled from the top, middle, and toe of a high-angle foreset. The Nipigon Bay Fm. was sampled from 3 cores at 229.5-, 390-, and 431.3-m stratigraphic depth. For each thin section, 24 images were stitched into a ~8 × 5 mm high-resolution digital mosaic of 0.685 pixels/μm. Two image mosaics were created from different areas of each thin section. Where visible, grain boundaries were manually identified and traced using Adobe Photoshop.

Measuring grain size from a 2-D thin section automatically biases size distributions finer because there is only one grain cross section reflecting the actual grain diameter. Sedimentologists counteract this bias by measuring the long axis of grains, and others sometimes use empirically based conversion equations (Friedman, 1958; Harrell & Eriksson, 1979) that have been met with skepticism (Johnson, 1994). Additionally, number counts are not as representative of volume/weight distributions. Hence, we used stereology.

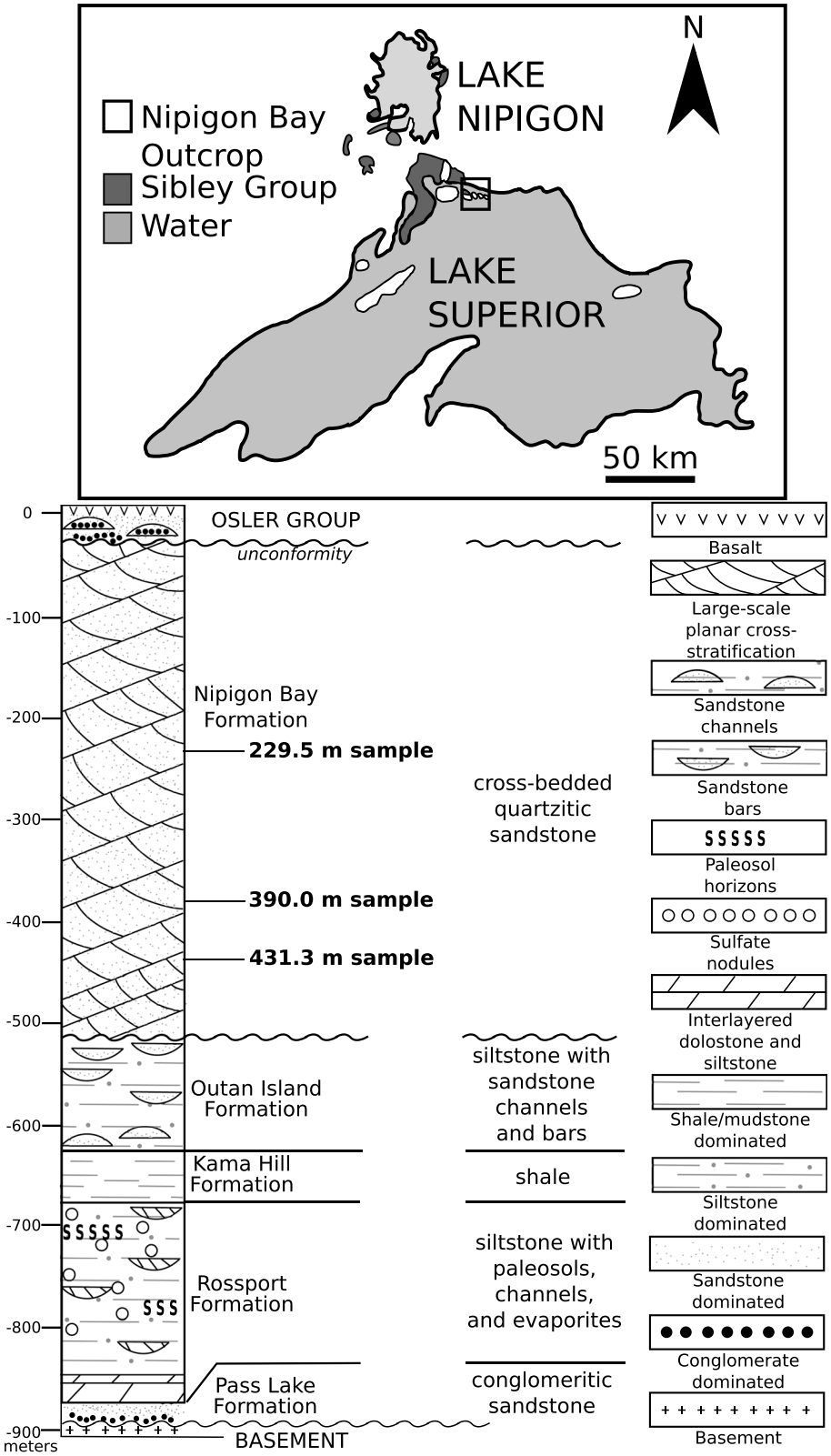

Figure 6. Location of the Sibley Basin and general stratigraphic column for the Sibley Group. Modified from Figures 1 and 2 in Rogala et al. (2007).

Stereology is a statistical technique used to convert 2-D distributions into representative 3-D volume distributions based on a relationship between surface area fraction and volume area fraction. It is used in multiple fields of microscopy, including cell biology and materials engineering. We specifically used a MATLAB® open-source stereology code formulated by Lehto et al. (2014) for size characterization of materials based on a point-sampled intercept method (Gundersen & Jensen, 1985; Underwood, 1973). For details, see Appendix B or Lehto et al. (2014).

Statistical measures of grain size were calculated using the logarithmic Folk and Ward (1957) graphical equations. We use the mean (M_Z) rather than the median because it more accurately represents the entire size of the distribution and is a better estimate of central tendency (Pettijohn et al., 1987). The inclusive graphical standard deviation on the mean (σ_I) is the sorting of grains based on both the central and exterior parts of the size distribution. Skewness (Sk_I) is the asymmetry of the distribution, reflecting the relative importance of the tails. Eolian dune sands are typically positively skewed (e.g., Ahlbrandt, 1979). Kurtosis (K_G) is the fit relative to a normal distribution. Grain sizes are in the phi scale ($\phi = -\log_2(d_{mm})$). Grain shape features were visually compared based on the Powers (1953) classification. See Appendix C for the descriptive terms. Statistical measures for each thin section were averaged to produce one value for the formation. Each sample was measured twice in different areas for robust grain counts and to ensure representative statistics. Descriptive sand sizes are based on the Wentworth (1922) scale.

6. Results

In thin sections, the Vryburg Fm. samples are compositionally mature, comprised principally of quartz with minor detrital orthoclase. Sericite, a white mica, is also present in small amounts. Grains of the original sandstone show poikilotopic syntaxial quartz overgrowth, suturing, and fracturing, producing an interlocking orthoquartzite fabric (Figures 7a and 7b). As a result, grains cannot be separated for grain surface analysis. Original boundaries, especially for the larger fraction, are semipreserved as inclusion trails in ~50% of grains and are visible in plane-polarized light (Figure 7a). The larger size fraction is well rounded to rounded and spherical, and the smaller size fraction is subrounded to subangular and less spherical. Additionally, thin sections revealed evidence of inverse grading from fine to coarse (Figure 7c). Lastly, a close-up view of a polished hand sample (Figure 7d) confirms the outcrop evidence of pinstripe lamination (Figure 5c).

Table 1 summarizes the statistical parameters for the Vryburg Fm. based on measurements of 1,759 grains. The distributions, shown in Figure 8 (black), are unimodal and grain sizes range from very fine (80 μm) up to the boundary between medium and coarse sand (500 μm), with a mean of 222 ± 8 μm (1σ). Sorting of grains is moderate (σ_I = 0.74), the distribution is slightly finely skewed (Sk_1 = 0.11) and is mesokurtic (K_G = 0.96), indicating it is approximately normal.

While the Nipigon Bay Fm. sandstone has undergone diagenetic alteration and quartz cementation, original grain boundaries are clearly preserved in thin section by clay and oxide coatings. Grains are compositionally fairly mature, with a majority of quartz but a significant fraction of orthoclase (Figures 7e and 7f). Table 1 also includes the statistical measures for the Nipigon Bay Fm. based on measurements of 3,422 grains. The distributions, shown in Figure 8 (gray), are unimodal and grain sizes range from very fine (70 μm) to medium sand (360 μm), with a mean of 191 ± 32 μm (1σ). Overall, grain sizes are moderately well sorted (σ_I = 0.55), with the distribution slightly finely skewed (Sk_1 = 0.18) and mesokurtic (K_G = 1.10), indicating it is approximately normal to slightly peaked. Grains are rounded to well rounded and show moderate to high sphericity.

7. Discussion

7.1. Depositional Environment Reconstruction

Distinguishing depositional environments based solely on statistical measures of grain size characteristics (e.g., Folk & Ward, 1957) should be met with skepticism (Pye & Tsoar, 1990). Determining the depositional origin of a sandstone requires both outcrop and grain scale observations. Conclusions about large-scale sedimentary features for the Precambrian sandstones that we studied are necessarily made from limited

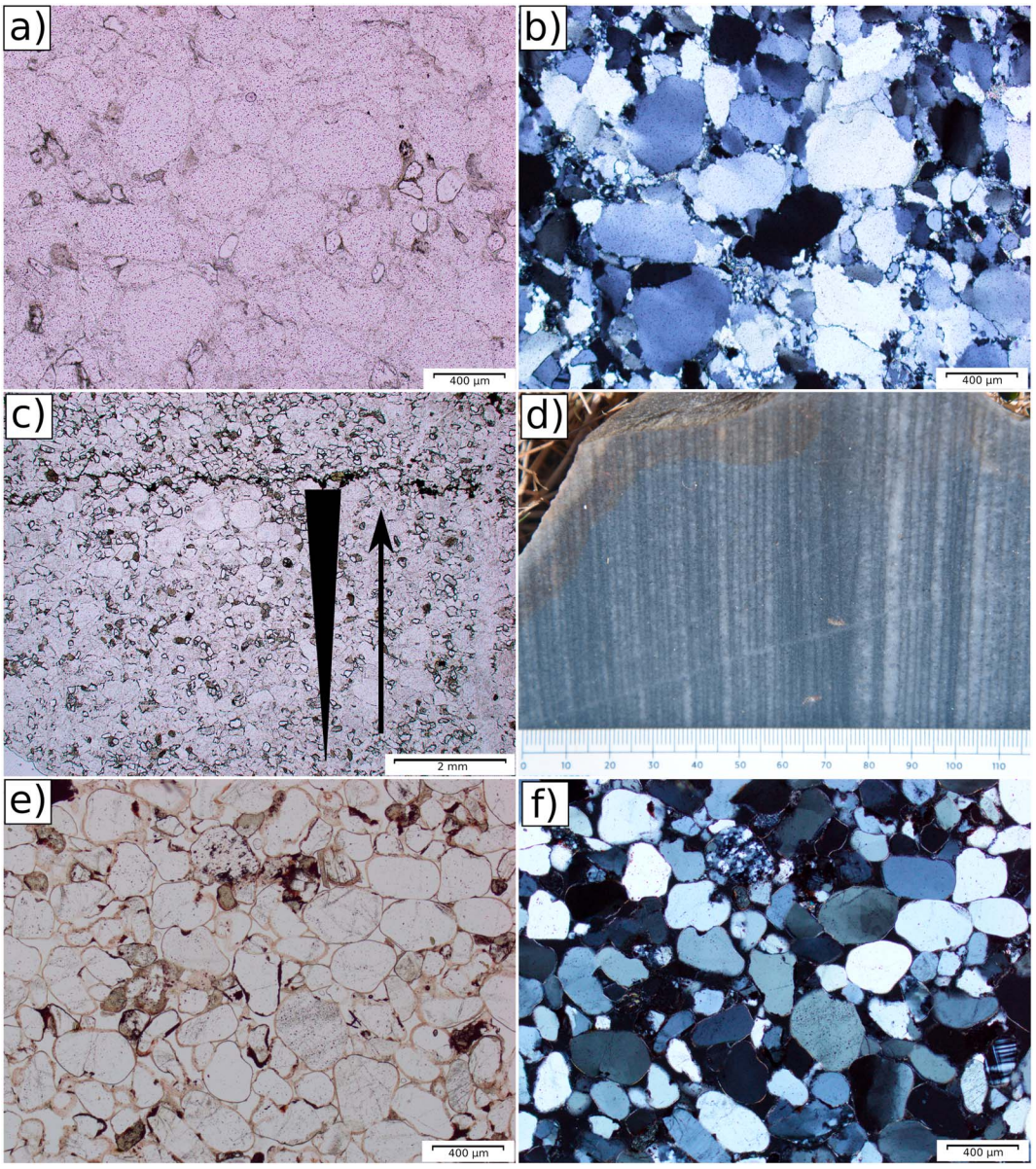

Figure 7. Photomicrographs of typical thin sections in plane-polarized (a) and cross-polarized light (b) for the Vryburg Fm. Original grain boundaries are visible in plane-polarized light for ~50% of grains. (c) Thin section showing inverse grading from fine to coarse grains. (d) Polished hand sample showing up-close pinstripe lamination. Photomicrographs of typical thin sections in plane-polarized light (e) and cross-polarized light (f) for the Nipigon Bay Fm. Scale bar in (a), (b), (e), and (f) is 400 µm. Scale bar in (c) is 2 mm. Scale in (d) is in millimeters.

outcrop exposure. Very large tabular crossbed sets with high-angle foresets are typical of eolian dunes. Tabular crossbeds for the Vryburg Fm. were observed up to 3 m in height and 20-m long. Sets of this size can be formed by both eolian dunes and fluvial dunes, explaining previous intertidal and fluvial interpretations (e.g., Beukes, 1986). However, outcrop and stratigraphic relationships in the area support an eolian origin. The Vryburg Fm. sandstones increase in maturity and in the size of crossbed sets upward. Basal conglomerates transition to fluvial trough crossbedded sandstones, marginal-marine, gray, feldspathic sandstones, and finally to the white, mature orthoquartzites described herein. Additionally, grainflow avalanche deposits at dune toes were observed at other outcrops, indicating eolian deposition (Anderson, 1988; Sutton et al., 2013).

Table 1
Results of Grain Size Analyses

Sample	Description	M_z (ϕ)	M_z (μm)	Range (μm)	σ_I (ϕ)	Sk_I (ϕ)	K_G (ϕ)	# of grains
V-1_1	Cross-set top	2.17	221	90–470	0.71	0.01	1.03	237
V-1_2	Cross-set top	2.21	216	90–430	0.70	0.11	0.94	321
V-2_1	Cross-set mid	2.22	214	90–450	0.72	0.12	0.99	269
V-2_2	Cross-set mid	2.20	218	90–450	0.69	0.09	1.05	263
V-3_1	Cross-set toe	2.12	227	80–500	0.81	0.13	0.88	346
V-3_2	Cross-set toe	2.10	233	90–500	0.79	0.20	0.88	323
Vryburg Fm.	—	***2.17***	***222***	***80–500***	***0.74***	***0.11***	***0.96***	***1,759***
NB-1_1	229.5-m core	2.17	222	100–350	0.52	0.23	1.13	388
NB-1_2	229.5-m core	2.18	220	110–360	0.51	0.20	1.10	426
NB-2_1	390.0-m core	2.27	207	90–350	0.56	0.16	1.07	445
NB2-_2	390.0-m core	2.32	200	90–360	0.59	0.14	1.01	592
NB-3_1	431.3-m core	2.68	156	70–260	0.54	0.20	1.15	612
NB-3_2	431.3-m core	2.72	150	70–260	0.56	0.16	1.13	959
Nipigon Bay Fm.	—	***2.39***	***191***	***70–360***	***0.55***	***0.18***	***1.10***	***3,422***

Note. Statistical measures for the Vryburg Fm. (labeled V-X_X) and Nipigon Bay Fm. (NB-X_X). Symbols are mean diameter M_z, inclusive graphical standard deviation σ_I, skewness Sk_I, and kurtosis K_G all as a function of size in the phi scale, ϕ. Bold values except range are averages for each formation. Range taken as the ϕ_5 and ϕ_{95} rounded to nearest multiple of 10. Bold range represents the size range of the entire set.

In the eolian section, millimeter-scale horizontal laminae (Figures 5c and 7d) are interpreted as pinstripe lamination, which are preferentially cemented laminations of fine grains that formed because silt and very fine sand were originally deposited in the troughs of migrating wind ripples (Fryberger & Schenk, 1988). Differential grain size resulted in the formation of pressure-solution cleavage during orthoquartzite recrystallization, now visible as the layered colors in the horizontal laminae. Additionally, thin sections revealed evidence of inverse grading from fine to coarse grains (Figure 7c). Both pinstripe lamination and inverse grading are distinctive features of eolian deposition.

Wind ripples are generally asymmetrical, low amplitude and have a high ripple index (wavelength/height >10; Wilson, 1972). The basal erosional features in the outcrop are overlain by low-index symmetrical ripples ~1 cm in height, suggesting the presence of extremely shallow water in a wet interdune setting. These transition into pinstripe lamination and the high-angle foresets, indicating the wet interdune segments were transient and graded to dry eolian processes.

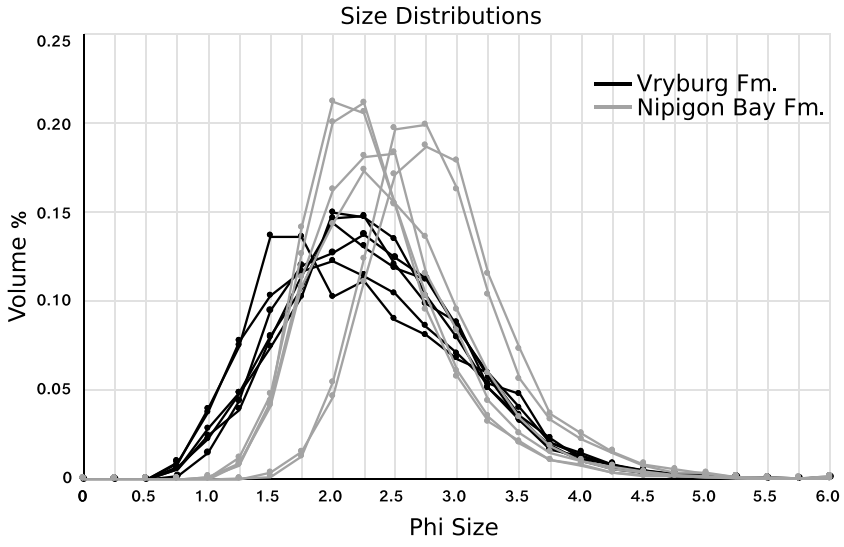

Figure 8. Size distributions of the Vryburg Fm. (black) and Nipigon Bay Fm. (gray). Data available at https://github.com/erikgoosmann/AeolianData.

Table 2
Results of Student's t Tests

Eolian Deposits and Elevation	Mean (μm)	Standard deviation	*n*	DoF	[a]t_{crit}	$\lvert t_{calc}\rvert$	Result
Modern Dunes	220	75	450	—	—	—	—
Vryburg Fm.	222	8	6	23	2.069	0.440	$p(\lvert t_{calc}\rvert > t_{crit}) > 0.05$; null hypothesis not rejected
Nipigon Bay Fm.	191	32	6	5	2.571	2.142	$p(\lvert t_{calc}\rvert > t_{crit}) > 0.05$; null hypothesis not rejected
Fan et al. (2010), 1,000 m	255	26	7	7	2.365	3.351	$p(\lvert t_{calc}\rvert > t_{crit}) < 0.05$; reject null hypothesis
Wiegand (1977), 2,500 m	236	47	137	137	1.977	8.674	$p(\lvert t_{calc}\rvert > t_{crit}) < 0.05$; reject null hypothesis
Hu et al. (2018), 3,500 m	184	47	61	106	1.982	5.158	$p(\lvert t_{calc}\rvert > t_{crit}) < 0.05$; reject null hypothesis
Hu et al. (2017), 4,200 m	182	19.7	58	324	1.967	2.435	$p(\lvert t_{calc}\rvert > t_{crit}) < 0.05$; reject null hypothesis

[a]t_{crit} is for a two-sided 95% confidence, *n* = sample size, and DoF = degrees of freedom. The null hypothesis is that the means are the same as the mean of the modern dunes.

At the grain scale for the Vryburg Fm., the moderate sorting and well-rounded to rounded larger grains is typical of eolian transport. The subangular nature of the smaller grains is possibly from postdepositional processes such as fracturing, and the lack of extreme rounding or sphericity for smaller grain sizes does not rule out an eolian origin. In modern eolian dunes, grain roundness and sphericity can decrease for the smaller size fraction (Khalaf & Gharib, 1985), as is observed in the Vryburg Fm.

Tabular crossbeds with high-angle foresets, pinstripe lamination, inverse grading, and the grain sizing all combine to support an eolian origin for the Vryburg Fm. crossbedded orthoquartzites at this locality. The Vryburg forms the base of a ~300-m fining cycle becoming marine upward (Figure 4), interpreted as the initial flooding of the Kaapvaal Craton and subsequent basin deepening (Altermann & Nelson, 1998; Schröder et al., 2006). The stratigraphic proximity of shallow, tidal, nearshore deposits suggests a coastal or upper beach environment for the Vryburg Fm. (Altermann et al., 2014), and basal low-index symmetrical ripples probably formed in shallow water in intermittently wet interdune areas. The overall depositional interpretation for the tabular crossbedded orthoquartzites is thus most likely a source-proximal coastal eolian environment.

This study's grain scale features corroborate the eolian origin for the Nipigon Bay Formation deduced from previous outcrop and drill core observations (Rogala et al., 2005; Rogala et al., 2007). There is a clear unconformity between the cross-stratified sandstone of the Nipigon Bay Fm. and the underlying fluvial conglomerate (Rogala et al., 2005). The Nipigon Bay Fm. outcrop on Simpson Island also exposes a large-scale remnant dune feature ~15 m in height (Rogala et al., 2005, 2007), which is rare in fluvial environments. Grains are rounded, subspherical, and moderately well sorted, further supporting wind transport. The depositional interpretation is a first-cycle eolianite due to the low compositional maturity.

7.2. Grain Size and Atmospheric Density

The measured mean grain sizes for the Vryburg (222 ± 8 μm) and the Nipigon Bay (191 ± 35 μm) Formations both fall within the 220 ± 75 μm (1σ) modern size range for sea level dunes on Earth (Ahlbrandt, 1979). Within the Nipigon Bay Formation there is a mean grain size difference of ~55 μm between sample NB-3 and the other two samples (NB-2 and NB-1), which is larger than the 31-μm size difference between the Nipigon Bay Fm. mean and the Vryburg Fm. mean. The Vryburg shows a larger size range than the Nipigon Bay, with sizes reaching up to coarse grained (>500 μm, Figure 8).

Student's *t* tests carried out on the grain measurements (Table 2) indicate that both the Vryburg Fm. and the Nipigon Bay Fm. cannot be statistically separated from the modern mean with 95% confidence. Given the paleopressure proxy measurement of 0.25–0.5 bar from Som et al. (2016) near the time of deposition of the Vryburg Formation, the results of this work indicate that either (1) decreasing modern atmospheric density by a factor of 2 to 4 is insufficient to cause a statistically significant change in the mean grain size of eolian dunes or (2) the late-Archean air density was closer to the maximum bound presented in the paleobarometric measurement of Som et al. (2016) or that of Avice et al. (2018).

Particle size distributions can vary within a dune field, between dune fields, and on individual dunes (e.g., Ahlbrandt, 1979). For this method to work as a paleopressure indicator, it requires a significant shift in sizes beyond natural eolian stochasticity, which is a product of many other factors such as source area, temperature, and wind regime. Importantly, air density and pressure differences required for a significant shift in mean grain size are probably larger than those available on Earth, even for high elevations. China's Ulan Buh Desert dunes at 1,000 m (~0.90 bar) have means of 255 ± 26 μm (Fan et al., 2010), Great Sand Dunes National Monument dunes at 2,500 m (~0.75 bar) have means of 236 ± 47 μm (Wiegand, 1977), and Tibetan Plateau early to late-Holocene dunes at 3,400 (~0.66 bar) and 4,230 m (~0.60 bar) have mean grain sizes of 184 ± 47 μm (Hu et al., 2018) and 182 ± 20 μm (Hu et al., 2017) respectively. All four sites at elevation are statistically different at 95% confidence compared to sea level dunes (Table 2). However, even the largest difference in means falls well within one standard deviation of the modern dunes. Given the 1σ spread for modern sand dunes is ±75 μm (Ahlbrandt, 1979), consistent grain sizes larger than the upper limit (295 μm) would be the minimum requirement for grain size change to be attributable to air density change. This would produce not only a statistically significant difference but also a practically significant difference in sizes compared to the modern sea level sand dune mean size.

Natural eolian stochasticity and the other end-member factors all contribute to mean grain size. In these elevated cases we cannot confidently attribute different mean grain size to air density change, especially given the lack of a systematic mean grain size trend, either coarser or finer, with increasing elevation. Evidently, any grain size variability in these dunes from an air density effect is masked by other physical processes. One possibility is source area complication. In the case of the Tibetan Plateau dunes at 4,200 and 3,500 m, the proximity of loess on the Plateau could be dominating the source area, thus making them finer. Additionally, air density decrease with elevation may also be negated, in part, by temperature decrease. This could affect the initiation of movement for sand grains. However, while lower temperature does increase air density proportionally, any reduction in threshold friction velocity from temperature decrease is matched by a decrease in kinematic viscosity of air of a similar magnitude (McKenna-Neuman, 2003). Nevertheless, temperature does have an effect on eolian transport, and it has been shown through wind tunnel observation that lower temperature increases the effectiveness of particle impacts and grain splash. The primary effect of lower temperature on eolian transport is the reduction of both the amount of water vapor in the air and the matric potential at which this water is adsorbed onto sand grains (McKenna-Neuman, 2004). Increased eolian transport with lower temperature could therefore be more of a result of increased bed elasticity during collisions, rather than from any air density increase.

If the paleobarometric measurement by Som et al. (2016) reflects an Archean air pressure that truly was 25% of modern levels, then ancient eolianites can sample eolian processes at greater density differences than available on the modern Earth. However, Figures 7a and 7b exemplify the inherent complexities of grain scale observations for Archean orthoquartzites that have undergone recrystallization. Yet it is difficult to make unequivocal conclusions about the utility of eolianite grain sizes as paleobarometers from single sites from 2.64 and 1.5 Ga. Grain sizes of other eolianites would help confirm the similar-to-modern mean grain size of eolianites for the middle to late Archean.

The most logical follow-up site deposited near in time to the Vryburg Formation and the Som et al. (2016) paleopressure measurement is the 2.7–2.4 Ga eolian sandstone member of the Tamanduá Group of the Minas Supergroup in Brazil (Simpson et al., 2004). While the 3.2 Ga Moodies Group has been reported to contain the world's oldest eolianite (Simpson et al., 2012), which is comparable in age to the Marty et al. (2013) and Avice et al. (2018) upper limits of 0.5–1.1 and 0.5–1 bar, respectively, many Moodies Group trough cross-bedded sandstones have been re-interpreted as tidal due to the presence of gutter casts (Homann et al., 2015). Another eolianite to consider is the Karutola Formation of the Dongargarh Supergroup in Central India (Chakraborty & Sensarma, 2008). However, the timing of deposition is not clearly constrained and broadly between the Neoarchean and Paleoproterozoic at around 2.5 Ga. Unfortunately, there are very few other identified Archean eolianites deposited near the time of the paleopressure measurements available in the literature, and most other known Precambrian eolianites are Proterozoic in age (Rodriguez-Lopez et al., 2014).

7.3. Applicability to Mars

Geologic proxies that effectively respond to changes in atmospheric density have implications beyond the atmospheric evolution of Earth. When considering eolian processes in a low-density atmosphere, Mars is a

good natural laboratory. Martian eolian bedforms have a trimodal wavelength distribution compared to Earth's current bimodal distribution, and middle-sized ripples with meter-scale wavelengths, sinuous crests, and angle of repose slopes on Mars are unlike typical centimeter-scale impact ripples and could be a result of the extremely thin atmosphere (Lapotre et al., 2016). These large ripples may follow scaling laws similar to fluvial drag ripples on Earth rather than typical eolian impact ripples. Additionally, the large ripples have similar orientations to impact ripples resulting from coincident formation (Ewing et al., 2017). While the large ripples observed at the Gobabeb site and upper High Dune site on Mars have similar grain sizes as the surrounding material and are dissimilar to coarse-grained ripples, observations of some large ripples at the base of High Dune have coarser-grained crests. With the presence of both on High Dune the exact formational process is unknown (i.e., two distinct mechanisms or a single mechanism with two end-members resulting from formation instability; Ewing et al., 2017). If these large ripples are a result of lower air density, wavelengths of these bedforms in the Martian geologic record could be used as tool for measuring atmospheric density over Mars' history (Lapotre et al., 2016) because Mars may have formed with a thicker atmosphere that has thinned over geologic time (Catling & Kasting, 2017, Chapter 12).

With the modern 6.1-mbar mean *surface level* Martian atmosphere (Haberle et al., 2008), 1 or 2 orders of magnitude in air density difference is not an unreasonable change over Martian geologic history. The lack of plate tectonics to metamorphose and recycle ancient rocks means that billion year old eolianites should be better preserved on Mars. Banham et al. (2018) identified the 3.7–3.0 Ga Stimson Formation sandstone as an ancient Martian eolianite and reported a 400 μm geometric mean size and a 285 μm modal mean size. Compared to the modern Bagnold Dunes these sizes are significantly larger than the ~100- to 125-μm mean size of the Martian Gobabeb and Otavi sample sites but is smaller than the 321-μm mean size from the Martian Barby sample site (Edwards et al., 2018; Ehlmann et al., 2017). Edwards et al. (2018) explain the grain size differences on the basis of whether samples were from lee or stoss sides of Martian dunes, where a stoss side or crest tends to have big grains and the lee side has smaller grains. However, variability between stoss and lee sides tends to be only a few microns or tens of microns for some terrestrial dunes (e.g., Purkait et al., 2015). For eolianites, lee sides tend to be more sampled because these are better preserved.

Importantly, grain size measurements are dependent on the method of calculating the mean (i.e. geometric, logarithmic, and modal). This can cause large differences in reported sizes, such as those for the Stimson Formation (400 and 285 μm). Generally, geometric (metric scale) and logarithmic (Phi scale) means are more informative for sediment transport because they scale the distribution to put equal weight on the small changes in the fine particles, thus giving a more representative value for the entire distribution. More samples from modern and ancient dunes on Mars, particularly from before 4.0 Ga when air density is thought to have been much higher on Mars, may indicate a coarsening or fining over geologic time and thus confirm the utility of grain size as a proxy on a planet that has had a larger magnitude air density change over time.

8. Conclusion

This is the first attempt to investigate quantitative grain size changes as a record of differences in air density during eolian transport from fossil sand dunes on Earth. The traditional theory of force balance suggests that air density change could affect mean grain sizes by extending the upper size limit of the grains capable of suspension during high speed gusts, leading to coarser pure saltation grain sizes and thus overall sand dune grain sizes. We analyzed grain sizes for two Precambrian eolianites, the ~2.64-Ga Vryburg Formation, deposited at a time with an atmospheric pressure between 1.1 and 0.25 bar (Som et al., 2012, 2016), and the ~1.5-Ga Nipigon Bay Formation, deposited during a time of unknown atmospheric pressure.

Grain-scale and outcrop-scale observations both support the eolian origin of the sandstone samples. The mean sizes of both the Vryburg Fm. and Nipigon Bay Fm. are within one standard deviation of those for modern eolian dunes, and Student's *t* tests at 95% confidence do not reject the null hypothesis that both the Vryburg Fm. and Nipigon Bay Fm. mean grain sizes are the same as the modern spread of sand dune mean grain sizes. Overall, this suggests that while air density is important in eolian physics, the relatively small deviations from 1 bar over Earth's history (suggested to be a factor of 2–4 either way in the literature; Goldblatt et al., 2009; Som et al., 2016) are likely insufficient to produce an unambiguous grain size

signal that can be separated from the natural variation in eolian sands. Sampling other late-Archean eolianites for grain sizes could confirm the similar-to-modern mean grain size during that time. Additionally, with possibly larger air density changes and better preservation potential, eolianites as an air density proxy may be more useful on Mars.

Appendix A: Distribution of Eolian Dune Mean Grain Sizes on the Modern Earth

Modern near-sea-level eolian dune fields composed of quartz sand mostly cluster around a similar mean grain size, especially when compared to fluvial sediments. This is true despite variable wind regimes, source areas, and dune types. Ahlbrandt (1979) compiled grain size distribution data for over 450 dunes around the world. Inland quartz dunes are generally coarser than coastal dunes, and coastal dunes are very well sorted while inland dunes are moderately well sorted. The differences are such that two populations are visible between the two dune types in the data (Ahlbrandt, 1979). However, this may reflect a sampling bias in the coastal dune population, as 218 of the 288 coastal dunes sampled were from a single dune field. Since both the Vryburg Fm. and Nipigon Bay Fm. eolianites used in this study are stratigraphically proximal to marine or lacustrine facies, and the exact relationship between most lithified eolianites and their proximity to the ocean is uncertain, the inland and coastal data sets were combined to calculate global averages for the grain size distribution statistics. Grain size statistics were averaged for each dune field when multiple dunes were sampled. Mean statistical measures were then calculated from the averages for the dune fields. Grain size data were ignored for ripples, nonquartz dominated dunes (e.g., White Sands National Monument), vegetated dunes (e.g., parabolic dunes), and high-altitude dunes (e.g., Great Sand Dunes National Monument). The resulting data set contained 404 dunes from 62 dune fields, and averaged to 220 ± 75 μm (1σ).

Appendix B: Stereology

To mitigate the bias of a random 2-D cross section of a 3-D grain, this stereology software (e.g., Lehto et al., 2014) calculates the volume-weighted mean grain size using a method of random point sampling. Each of the random 20,000 points measures grain diameter at one of four evenly spaced directions (0°, 45°, 90°, and 135°). For each of the random points, a grain diameter of size *i* has a probability of being *hit* that is proportional to the surface area fraction. Creating an accurate 3-D distribution from a 2-D one relies on this statistical relationship between surface area fraction and volume fraction, such that the probability of hitting a grain of size *i* is directly proportional to surface area ratio and volume ratio:

$$P_i = \frac{A_i}{A_T} \approx \frac{V_i}{V_T} \tag{B1}$$

This means that the surface area fraction is a good estimator of the true volume fraction (Underwood, 1973). When *n* size measurements overall are taken using the point-sampled method, a size distribution is created where the frequency of occurrences of grain size *i* is determined by the probability of being measured:

$$n_i = nP_i = n\frac{V_i}{V_T} \tag{B2}$$

The arithmetic mean is then calculated:

$$d_v = \frac{1}{n}\sum_{i=1}^{n} n_i d_i \tag{B3}$$

Through substitution of equation (B2) into equation (B3), the volume-weighted average grain size is

$$d_v = \frac{1}{n}\sum_{i=1}^{n} n\frac{V_i}{V_T} d_i = \frac{1}{V_T}\sum_{i=1}^{n} V_i d_i \tag{B4}$$

The volume-weighted average grain size is thus calculated by weighting each measurement based on corresponding grain volume percent. At high *n*, this method is shown to accurately capture distribution tails (Lehto et al., 2014).

Appendix C: Statistical Measures and Roundness Definitions and Terminology

Standard verbal and quantitative terms (Figure C1a) were used to statistically describe the Vryburg Fm., Nipigon Bay Fm., and modern sand dune grain size distributions. Visual guidelines (Figure C1b) were used to describe grain shapes.

a

Mean	Sorting	Skewness	Kurtosis
$M_Z = \frac{\phi_{16} + \phi_{50} + \phi_{84}}{3}$	$\sigma_I = \frac{\phi_{84} - \phi_{16}}{4} + \frac{\phi_{95} - \phi_5}{6.6}$	$Sk_I = \frac{\phi_{16} + \phi_{84} - 2\phi_{50}}{2(\phi_{84} - \phi_{16})} + \frac{\phi_5 + \phi_{95} - 2\phi_{50}}{2(\phi_{95} - \phi_5)}$	$K_G = \frac{\phi_{95} + \phi_5}{2.44(\phi_{75} - \phi_{25})}$

Sorting (σ_I)		Skewness (Sk_I)		Kurtosis (K_G)	
Very well sorted	<0.35	Very fine skewed	+0.3 to +1.0	Very platykurtic	<0.67
Well sorted	0.35-0.50	Fine skewed	+0.1 to +0.3	Platykurtic	0.67-0.90
Moderately well sorted	0.50-0.70	Symmetrical	+0.1 to -0.1	Mesokurtic	0.90-1.11
Moderately sorted	0.70-1.00	Coarse skewed	-0.1 to -0.3	Leptokurtic	1.11-1.50
Poorly sorted	1.00-2.00	Very coarse skewed	-0.3 to -1.0	Very leptokurtic	1.50 - 3.00
Very poorly sorted	2.00-4.00			Extremely leptokurtic	>3.00
Extremely poorly sorted	>4.00				

b

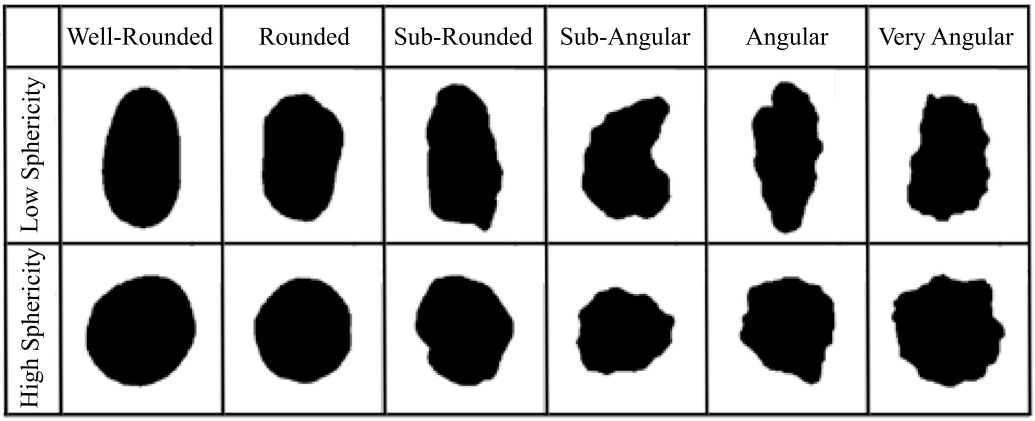

Figure C1. (a) Descriptions of statistical measures, following Blott and Pye (2001). (b) Visual classification of grain shape, following Powers (1953).

Acknowledgments

The authors thank Philip Fralick for providing the Nipigon Bay Fm. photographs, Eva Stüeken and Philip Fralick for providing the Nipigon Bay Fm. drill core samples, MacKenzie Day for her insightful comments, and Ed Simpson and Steve Banham for their critical reviews. This work was supported by the Simons Collaboration on the Origin of Life Award 511570 to D. C. C. and by the NASA Astrobiology Institute's Virtual Planetary Laboratory, grant NNA13AA93A. A digitized version of the Ahlbrandt (1979) global dune dataset and data for distributions in Figure are available at https://github.com/erikgoosmann/AeolianData.

References

Ahlbrandt, T. S. (1979). Textural parameters of eolian deposits. In *A study of global sand seas*, edited, *United States Geological Survey Professional Paper*, (pp. 21–51). Washington, D.C: U.S. Government Printing Office.

Altermann, W., Corcoran, P. L., & Mohlahlana, N. (2014). Aeolian beach deposits in the 2.64 Ga Vryburg formation, Griqualand West, South Africa, paper presented at 2014 GSA Annual Meeting in Vancouver, British Columbia.

Altermann, W., & Nelson, D. R. (1998). Sedimentation rates, basin analysis and regional correlations of three Neoarchaean and Palaeoproterozoic sub-basins of the Kaapvaal craton as inferred from precise U–Pb zircon ages from volcaniclastic sediments. *Sedimentary Geology*, *120*(1–4), 225–256. https://doi.org/10.1016/S0037-0738(98)00034-7

Anderson, R. S. (1988). The pattern of grainfall deposition in the lee of aeolian dunes. *Sedimentology*, *35*(2), 175–188. https://doi.org/10.1111/j.1365-3091.1988.tb00943.x

Avice, G., Marty, B., Burgess, R., Hofmann, A., Philippot, P., Zahnle, K., & Zakharov, D. (2018). Evolution of atmospheric xenon and other noble gases inferred from Archean to Paleoproterozoic rocks. *Geochimica et Cosmochimica Acta*, *232*, 82–100. https://doi.org/10.1016/j.gca.2018.04.018

Bagnold, R. A. (1941). *The physics of blown sand and desert dunes*, (p. 265). London: Methuen & co.

Bagnold, R. A. (1966). An approach to the sediment transport problem from general physics, US government printing office.

Banham, S., Gupta, S., Rubin, D. M., Watkins, J. A., Sumner, D. Y., Edgett, K. S., et al. (2018). Ancient Martian aeolian processes and palaeomorphology reconstructed from the Stimson formation on the lower slope of Aeolis Mons, Gale crater, Mars. *Sedimentology*, *65*(4), 993–1042. https://doi.org/10.1111/sed.12469

Bekker, A., Holland, H., Wang, P.-L., Rumble Iii, D., Stein, H., Hannah, J., et al. (2004). Dating the rise of atmospheric oxygen. *Nature*, *427*(6970), 117–120. https://doi.org/10.1038/nature02260

Berner, R. A. (2006). Geological nitrogen cycle and atmospheric N2 over Phanerozoic time. *Geology*, *34*(5), 413–415. https://doi.org/10.1130/G22470.1

Beukes, N. (1986). The Transvaal sequence in Griqualand west. *Mineral deposits of southern Africa*, *1*, 819–828.

Blott, S. J., & Pye, K. (2001). GRADISTAT: A grain size distribution and statistics package for the analysis of unconsolidated sediments. *Earth Surface Processes and Landforms*, *26*(11), 1237–1248. https://doi.org/10.1002/esp.261

Catling, D. C., & Kasting, J. F. (2017). *Atmospheric evolution on inhabited and lifeless worlds*, (p. 592). Cambridge: Cambridge University Press.

Chakraborty, T., & Sensarma, S. (2008). Shallow marine and coastal eolian quartz arenites in the Neoarchean-Paleoproterozoic Karutola Formation, Dongargarth Volcano-sedimentary succession, central India. *Precambrian Research*, *162*(1–2), 284–301. https://doi.org/10.1016/j.precamres.2007.07.024

Claudin, P., & Andreotti, B. (2006). A scaling law for aeolian dunes on Mars, Venus, earth, and for subaqueous ripples. *Earth and Planetary Science Letters*, *252*(1–2), 30–44. https://doi.org/10.1016/j.epsl.2006.09.004

Eastwood, E. N., Kocurek, G., Mohrig, D., & Swanson, T. (2012). Methodology for reconstructing wind direction, wind speed and duration of wind events from aeolian cross-strata. *Journal of Geophysical Research*, *117*, F03035. https://doi.org/10.1029/2012jf002368

Edgett, K. S., & Christensen, P. R. (1991). The particle-size of Martian aeolian dunes. *Journal of Geophysical Research*, *96*(E5), 22,765–22,776. https://doi.org/10.1029/91je02412

Edwards, C. S., Piqueux, S., Hamilton, V. E., Fergason, R. L., Herkenhoff, K. E., Vasavada, A. R., et al. (2018). The thermophysical properties of the Bagnold dunes, Mars: Ground-truthing orbital data. *Journal of Geophysical Research: Planets*, *123*, 1307–1326. https://doi.org/10.1029/2017JE005501

Ehlmann, B., Edgett, K., Sutter, B., Achilles, C., Litvak, M., Lapotre, M., et al. (2017). Chemistry, mineralogy, and grain properties at Namib and high dunes, Bagnold dune field, Gale crater, Mars: A synthesis of curiosity rover observations. *Journal of Geophysical Research: Planets*, *122*, 2510–2543. https://doi.org/10.1002/2017JE005267

Eriksson, P., Altermann, W., & Hartzer, F. (2006). *The Transvaal Supergroup and its precursors*, (pp. 237–260). Pretoria: The Geology of South Africa.

Ewing, R., Lapotre, M., Lewis, K., Day, M., Stein, N., Rubin, D., et al. (2017). Sedimentary processes of the Bagnold dunes: Implications for the eolian rock record of Mars. *Journal of Geophysical Research: Planets*, *122*, 2544–2573. https://doi.org/10.1002/2017JE005324

Fan, Y., Chen, F., Fan, T., Zhao, H., & Yang, L. (2010). Sedimentary documents and optically stimulated luminescence (OSL) dating for formation of the present landform of the northern Ulan Buh Desert, northern China. *Science China Earth Sciences*, *53*(11), 1675–1682. https://doi.org/10.1007/s11430-010-3085-1

Ferguson, R., & Church, M. (2004). A simple universal equation for grain settling velocity. *Journal of Sedimentary Research*, *74*(6), 933–937. https://doi.org/10.1306/051204740933

Folk, R. L., & Ward, W. C. (1957). Brazos River bar: A study in the significance of grain size parameters. *Journal of Sedimentary Research*, *27*(1), 3–26. https://doi.org/10.1306/74D70646-2B21-11D7-8648000102C1865D

Friedman, G. M. (1958). Determination of sieve-size distribution from thin-section data for sedimentary petrological studies. *The Journal of Geology*, *66*(4), 394–416. https://doi.org/10.1086/626525

Fryberger, S. G., & Schenk, C. J. (1988). Pin stripe lamination: A distinctive feature of modern and ancient eolian sediments. *Sedimentary Geology*, *55*(1–2), 1–15. https://doi.org/10.1016/0037-0738(88)90087-5

Gatlin, P. N., Thurai, M., Bringi, V., Petersen, W., Wolff, D., Tokay, A., et al. (2015). Searching for large raindrops: A global summary of two-dimensional video disdrometer observations. *Journal of Applied Meteorology and Climatology*, *54*(5), 1069–1089. https://doi.org/10.1175/JAMC-D-14-0089.1

Goldblatt, C., Claire, M. W., Lenton, T. M., Matthews, A. J., Watson, A. J., & Zahnle, K. J. (2009). Nitrogen-enhanced greenhouse warming on early earth. *Nature Geoscience*, *2*(12), 891–896. https://doi.org/10.1038/ngeo692

Goudie, A., Warren, A., Jones, D., & Cooke, R. (1987). The character and possible origins of the aeolian sediments of the Wahiba Sand Sea, Oman. *Geographical Journal*, *153*(2), 231–256. https://doi.org/10.2307/634875

Greeley, R., & Iversen, J. D. (1985). *Wind as a geological process: on Earth, Mars, Venus, and Titan*, (p. 348). Cambridge Cambridgeshire; New York: Cambridge University press.

Gundersen, H., & Jensen, E. (1985). Stereological estimation of the volume-weighted mean volume of arbitrary particles observed on random sections. *Journal of Microscopy*, *138*(2), 127–142. https://doi.org/10.1111/j.1365-2818.1985.tb02607.x

Haberle, R. M., Forget, F., Colaprete, A., Schaeffer, J., Boynton, W. V., Kelly, N. J., & Chamberlain, M. A. (2008). The effect of ground ice on the Martian seasonal CO2 cycle. *Planetary and Space Science*, *56*(2), 251–255. https://doi.org/10.1016/j.pss.2007.08.006

Harrell, J., & Eriksson, K. (1979). Empirical conversion equations for thin-section and sieve derived size distribution parameters. *Journal of Sedimentary Research*, *49*(1), 0273–0280.

Holland, H. D. (2002). Volcanic gases, black smokers, and the great oxidation event. *Geochimica et Cosmochimica Acta*, *66*(21), 3811–3826. https://doi.org/10.1016/S0016-7037(02)00950-X

Homann, M., Heubeck, C., Airo, A., & Tice, M. M. (2015). Morphological adaptations of 3.22 Ga-old tufted microbial mats to Archean coastal habitats (Moodies group, Barberton Greenstone Belt, South Africa). *Precambrian Research*, *266*, 47–64. https://doi.org/10.1016/j.precamres.2015.04.018

Hu, G., Yu, L., Dong, Z., Jin, H., Luo, D., Wang, Y., & Lai, Z. (2017). Holocene aeolian activity in the headwater region of the Yellow River, Northeast Tibet plateau, China: A first approach by using OSL-dating. *Catena*, *149*, 150–157. https://doi.org/10.1016/j.catena.2016.09.014

Hu, G., Yu, L., Dong, Z., Lu, J., Li, J., Wang, Y., & Lai, Z. (2018). Holocene aeolian activity in the Zoige Basin, northeastern Tibetan plateau, China. *Catena*, *160*, 321–328. https://doi.org/10.1016/j.catena.2017.10.005

Iversen, J. D., & White, B. R. (1982). Saltation threshold on earth, Mars and Venus. *Sedimentology*, *29*(1), 111–119. https://doi.org/10.1111/j.1365-3091.1982.tb01713.x

Jerolmack, D. J., Mohrig, D., Grotzinger, J. P., Fike, D. A., & Watters, W. A. (2006). Spatial grain size sorting in eolian ripples and estimation of wind conditions on planetary surfaces: Application to Meridiani Planum, Mars. *Journal of Geophysical Research*, *111*, E12S02. https://doi.org/10.1029/2005JE002544

Johnson, B., & Goldblatt, C. (2015). The nitrogen budget of earth. *Earth-Science Reviews*, *148*, 150–173. https://doi.org/10.1016/j.earscirev.2015.05.006

Johnson, M. (1994). Thin section grain size analysis revisited. *Sedimentology*, *41*(5), 985–999. https://doi.org/10.1111/j.1365-3091.1994.tb01436.x

Kavanagh, L., & Goldblatt, C. (2015). Using raindrops to constrain past atmospheric density. *Earth and Planetary Science Letters*, *413*, 51–58. https://doi.org/10.1016/j.epsl.2014.12.032

Khalaf, F., & Gharib, I. (1985). Roundness parameters of quartz grains of recent aeolian sand deposits in Kuwait. *Sedimentary Geology*, *45*(1–2), 147–158. https://doi.org/10.1016/0037-0738(85)90028-4

Kocurek, G. (1996). Desert aeolian systems. In H. G. Reading (Ed.), *Sedimentary environments: Processes, facies and stratigraphy*, edited by, (pp. 125–133). Oxford: Blackwell.

Kok, J. F. (2010). Difference in the wind speeds required for initiation versus continuation of sand transport on Mars: Implications for dunes and dust storms. *Physical Review Letters*, *104*(7). https://doi.org/10.1103/PhysRevLett.104.074502

Kok, J. F., Parteli, E. J. R., Michaels, T. I., & Karam, D. B. (2012). The physics of wind-blown sand and dust. *Reports on Progress in Physics*, *75*(10), 106901. https://doi.org/10.1088/0034-4885/75/10/106901

Kok, J. F., & Renno, N. O. (2009). A comprehensive numerical model of steady state saltation (COMSALT). *Journal of Geophysical Research*, *114*, D17204. https://doi.org/10.1029/2009JD011702

Komabayasi, M., Gonda, T., & Isono, K. (1964). Life time of water drops before breaking and size distribution of fragment droplets. *Journal of the Meteorological Society of Japan. Ser. II*, *42*(5), 330–340. https://doi.org/10.2151/jmsj1923.42.5_330

Krissansen-Totton, J., Arney, G. N., & Catling, D. C. (2018). Constraining the climate and ocean pH of the early earth with a geological carbon cycle model. *Proceedings of the National Academy of Sciences*, *115*(16), 4105–4110. https://doi.org/10.1073/pnas.1721296115

Lancaster, N. (1995). *Geomorphology of desert dunes*, (p. 290). London; New York: Routledge.

Laneuville, M., Kameya, M., & Cleaves, H. J. (2018). Earth without life: A systems model of a global abiotic nitrogen cycle. *Astrobiology*, *18*(7). https://doi.org/10.1089/ast.2017.1700

Lapotre, M., Ewing, R., Lamb, M., Fischer, W., Grotzinger, J., Rubin, D., et al. (2016). Large wind ripples on Mars: A record of atmospheric evolution. *Science*, *353*(6294), 55–58. https://doi.org/10.1126/science.aaf3206

Lehto, P., Remes, H., Saukkonen, T., Hanninen, H., & Romanoff, J. (2014). Influence of grain size distribution on the Hall-Petch relationship of welded structural steel. *Impact Factor of Materials Science And Engineering A-Structural*, *592*, 28–39. https://doi.org/10.1016/j.msea.2013.10.094

Lorenz, R. D. (1996). Martian surface wind speeds described by the Weibull distribution. *Journal of Spacecraft and Rockets*, *33*(5), 754–756. https://doi.org/10.2514/3.26833

Lorenz, R. D., Bridges, N. T., Rosenthal, A. A., & Donkor, E. (2014). Elevation dependence of bedform wavelength on Tharsis Montes, Mars: Atmospheric density as a controlling parameter. *Icarus*, *230*(Supplement C), 77–80. https://doi.org/10.1016/j.icarus.2013.10.026

Mallik, A., Li, Y., & Wiedenbeck, M. (2018). Nitrogen evolution within the Earth's atmosphere–mantle system assessed by recycling in subduction zones. *Earth and Planetary Science Letters*, *482*, 556–566. https://doi.org/10.1016/j.epsl.2017.11.045

Marty, B., Zimmermann, L., Pujol, M., Burgess, R., & Philippot, P. (2013). Nitrogen isotopic composition and density of the Archean atmosphere. *Science*, *342*(6154), 101–104. https://doi.org/10.1126/science.1240971

McKenna-Neuman, C. (2003). Effects of temperature and humidity upon the entrainment of sedimentary particles by wind. *Boundary-Layer Meteorology*, *108*(1), 61–89. https://doi.org/10.1023/A:1023035201953

McKenna-Neuman, C. (2004). Effects of temperature and humidity upon the transport of sedimentary particles by wind. *Sedimentology*, *51*(1), 1–17. https://doi.org/10.1046/j.1365-3091.2003.00604.x

Musiolik, G., Kruss, M., Demirci, T., Schrinski, B., Teiser, J., Daerden, F., et al. (2018). Saltation under Martian gravity and its influence on the global dust distribution. *Icarus*, *306*, 25–31. https://doi.org/10.1016/j.icarus.2018.01.007

Pettijohn, F. J., Potter, P. E., & Siever, R. (1987). *Sand and sandstone*, (2nd ed.p. 553). Berlin: Springer Science & Business Media.

Powers, M. C. (1953). A new roundness scale for sedimentary particles. *Journal of Sedimentary Research*, *23*(2), 117–119.

Purkait, B., Majumdar, D. D., & Paul, A. K. (2015). Grain sorting on a coastal dune of Orissa, bay of Bengal and a comparison with the desert dune of Rajasthan, India. *International Research Journal of Earth Sciences*, *3*(8), 14–31.

Pye, K. (1987). *Aeolian dust and dust deposits*.

Pye, K., & Tsoar, H. (1990). *Aeolian sand and sand dunes*, (p. 396). London; Boston.: Unwin Hyman.

Rodriguez-Lopez, J. P., Clemmensen, L. B., Lancaster, N., Moutney, N. P., & Veiga, G. D. (2014). Archean to recent aeolian sand systems and their sedimentary record: Current understanding and future prospects. *Sedimentology*, *61*(6), 1487–1534. https://doi.org/10.1111/sed.12123

Rogala, B., Fralick, P. W., Heaman, L. M., & Metsaranta, R. (2007). Lithostratigraphy and chemostratigraphy of the Mesoproterozoic Sibley Group, northwestern Ontario, Canada. *Canadian Journal of Earth Sciences*, *44*(8), 1131–1149. https://doi.org/10.1139/e07-027

Rogala, B., Fralick, P. W., & Metsaranta, R. (2005). Stratigraphy and sedimentology of the Mesoproterozoic Sibley Group and related igneous intrusions, northwestern Ontario: Lake Nipigon Region Geoscience Initiative, 128 pp., Ontario Geological Survey.

Schröder, S., Lacassie, J. P., & Beukes, N. J. (2006). Stratigraphic and geochemical framework of the Agouron drill cores, Transvaal Supergroup (Neoarchean–Paleoproterozoic, South Africa). *South African Journal of Geology*, *109*(1–2), 23–54. https://doi.org/10.2113/gssajg.109.1-2.23

Shao, Y. (2008). *Physics and modelling of wind erosion*, (p. 456). Berlin: Springer Science & Business Media.

Shao, Y. P., & Klose, M. (2016). A note on the stochastic nature of particle cohesive force and implications to threshold friction velocity for aerodynamic dust entrainment. *Aeolian Research*, *22*, 123–125. https://doi.org/10.1016/j.aeolia.2016.08.004

Shao, Y. P., & Lu, H. (2000). A simple expression for wind erosion threshold friction velocity. *Journal of Geophysical Research*, *105*(D17), 22,437–22,443. https://doi.org/10.1029/2000jd900304

Simpson, E., Alkmim, F., Bose, P., Bumby, A., Eriksson, K., Eriksson, P., et al. (2004). Sedimentary dynamics of Precambrian aeolianites. In *The Precambrian Earth: tempos and events*, (pp. 642–657). Amsterdam: Elsevier.

Simpson, E. L., Eriksson, K. A., & Mueller, W. U. (2012). 3.2 Ga eolian deposits from the Moodies Group, Barberton Greenstone Belt, South Africa: Implications for the origin of first-cycle quartz sandstones. *Precambrian Research*, *214-215*, 185–191. https://doi.org/10.1016/j.precamres.2012.01.019

Som, S. M., Buick, R., Hagadorn, J. W., Blake, T. S., Perreault, J. M., Harnmeijer, J. P., & Catling, D. C. (2016). Earth's air pressure 2.7 billion years ago constrained to less than half of modern levels. *Nature Geoscience*, *9*(6), 448–451. https://doi.org/10.1038/ngeo2713

Som, S. M., Catling, D. C., Harnmeijer, J. P., Polivka, P. M., & Buick, R. (2012). Air density 2.7 billion years ago limited to less than twice modern levels by fossil raindrop imprints. *Nature*, *484*(7394), 359–362. https://doi.org/10.1038/nature10890

Stüeken, E. E., Kipp, M. A., Koehler, M. C., Schwieterman, E. W., Johnson, B., & Buick, R. (2016). Modeling pN2 through geological time: Implications for planetary climates and atmospheric biosignatures. *Astrobiology*, *16*(12), 949–963. https://doi.org/10.1089/ast.2016.1537

Sullivan, R., & Kok, J. (2017). Aeolian saltation on Mars at low wind speeds. *Journal of Geophysical Research: Planets*, *122*, 2111–2143. https://doi.org/10.1002/2017JE005275

Sutton, S. L. F., McKenna, N. C., & Nickling, W. (2013). Avalanche grainflow on a simulated aeolian dune. *Journal of Geophysical Research: Earth Surface*, *118*, 1767–1776. https://doi.org/10.1002/jgrf.20130

Telfer, M. W., Parteli, E. J. R., Radebaugh, J., Beyer, R. A., Bertrand, T., Forget, F., et al. (2018). Dunes on Pluto. *Science*, *360*(6392), 992–997. https://doi.org/10.1126/science.aao2975

Underwood, E. E. (1973). Quantitative stereology for microstructural analysis. In *Microstructural Analysis*, edited, (pp. 35–66). New York: Springer.

Walraven, F., & Martini, J. (1995). Zircon Pb-evaporation age determinations of the Oak Tree Formation, Chuniespoort group, Transvaal sequence: Implications for Transvaal-Griqualand West basin correlations. *South African Journal of Geology*, *98*(1), 58–67.

Wentworth, C. K. (1922). A scale of grade and class terms for clastic sediments. *The Journal of Geology*, *30*(5), 377–392. https://doi.org/10.1086/622910

Wiegand, J. P. (1977). Dune morphology and sedimentology at Great Sand Dunes National Monument, 165 pp., MS Thesis, Colorado State University.

Wilson, I. G. (1972). Aeolian bedforms—Their development and origins. *Sedimentology*, *19*(3–4), 173–210. https://doi.org/10.1111/j.1365-3091.1972.tb00020.x

Zahnle, K., Claire, M., & Catling, D. (2006). The loss of mass-independent fractionation in sulfur due to a Palaeoproterozoic collapse of atmospheric methane. *Geobiology*, *4*(4), 271–283. https://doi.org/10.1111/j.1472-4669.2006.00085.x